Open Access on 07/14/2015

Chelator-Free ^{64}Cu-Integrated Gold Nanomaterials for Positron Emission Tomography Imaging Guided Photothermal Cancer Therapy

Xiaolian Sun,[†,‡,*] Xinglu Huang,[†] Xuefeng Yan,[†] Yu Wang,[†] Jinxia Guo,[†,‡] Orit Jacobson,[†] Dingbin Liu,[†] Lawrence P. Szajek,[§] Wenlei Zhu,[∥] Gang Niu,[†] Dale O. Kiesewetter,[†] Shouheng Sun,[∥] and Xiaoyuan Chen[†,*]

[†]Laboratory of Molecular Imaging and Nanomedicine (LOMIN), National Institute of Biomedical Imaging and Bioengineering (NIBIB), National Institutes of Health, Bethesda, Maryland 20892, United States, [‡]Center for Molecular Imaging and Translational Medicine, School of Public Health, Xiamen University, Xiamen 261005, China, [§]Positron Emission Tomography Department, Warren Grant Magnuson Clinical Center, National Institutes of Health, Bethesda, Maryland 20892, United States, and [∥]Department of Chemistry, Brown University, Providence, Rhode Island 02912, United States

ABSTRACT Using positron emission tomography (PET) imaging to monitor and quantitatively analyze the delivery and localization of Au nanomaterials (NMs), a widely used photothermal agent, is essential to optimize therapeutic protocols to achieve individualized medicine and avoid side effects. Coupling radiometals to Au NMs *via* a chelator faces the challenges of possible detachment of the radiometals as well as surface property changes of the NMs. In this study, we reported a simple and general chelator-free ^{64}Cu radiolabeling method by chemically reducing ^{64}Cu on the surface of polyethylene glycol (PEG)-stabilized Au NMs regardless of their shape and size. Our ^{64}Cu-integrated NMs are proved to be radiochemically stable and can provide an accurate and sensitive localization of NMs through noninvasive PET imaging. We further integrated ^{64}Cu onto arginine-glycine-aspartic acid (RGD) peptide modified Au nanorods (NRs) for tumor theranostic application. These NRs showed high tumor targeting ability in a U87MG glioblastoma xenograft model and were successfully used for PET image-guided photothermal therapy.

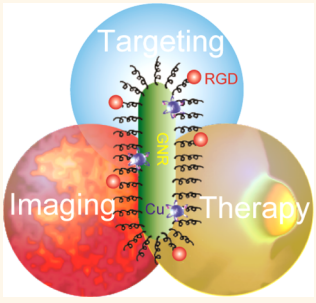

KEYWORDS: ^{64}Cu labeling · chelator free · PET · image-guided photothermal therapy

Imaging-guided therapy, which bridges diagnosis and therapy, is significant in solving the challenges of cancer heterogeneity and adaptation. The knowledge of the exact location of the tumor is essential to provide therapeutic treatments that are more specific to individuals and, thus, enhance the therapeutic efficiency and reduce side effects to nearby organs.[1−3] To achieve this goal, a multifunctional probe should be designed to be target-specific and to serve as both an imaging enhancer and a therapeutic agent.

Au nanomaterials (NMs) have been widely used in the theranostic field because of their biocompatibility, stability, and facile conjugation with biomolecules. Their unique physical properties make them potential CT, Raman spectroscopy, and photoacoustic imaging agents.[4−6] The ability of Au NMs to absorb light and efficiently convert the light into heat has been employed for the thermal ablation of tumors.[6] This so-called photothermal therapy (PTT) application of Au NMs upon the addition of a laser source has been well established in the cancer therapy field. However, it is always a challenge to limit the generated heat to focus on the tumor area and control the laser power to minimize the side effects to normal surrounding tissue. Until now, the most widely used countermeasure is to introduce Au NMs *via* intratumoral injection and to confine the laser exposure area. However, for intravenous (iv) injections, which have more practical clinical value, information on the pharmacokinetics and distribution of the injected particles is critically needed to decide when, where, and how to apply the laser.

Among all the diagnostic imaging methods, radionuclide-based positron emission tomography (PET) imaging has its unique advantages of high sensitivity and the ability to conduct quantitative analysis of whole-body images.[7−9] To integrate PET imaging capability into Au NMs, the most

* Address correspondence to xiaolian.sun@nih.gov; shawn.chen@nih.gov.

Received for review May 30, 2014 and accepted July 14, 2014.

Published online July 14, 2014
10.1021/nn502950t

common way is to attach a radiometal (*e.g.*, ^{64}Cu) onto the Au NMs *via* a metal chelator.[10−12] However, the attachment of radiometal−chelator complexes will influence the surface properties of the NMs and reduce the capability of loading other targeting or therapeutic agents. The possible detachment of the radiometal by either transchelation of the radiometal from the chelator complex or the dissociation of the radionuclide-containing polymer coating from the nanoparticle in the presence of high protein concentration could also lead to a significant difference between the radionuclide signal and the distribution of NMs. Intrinsically radioactive NMs prepared by either chemical incorporation of a radioisotope into the NMs[13] or physical assembly of radiolabeled building blocks[14,15] have been proved to be able to avoid these limitations. Radioactive ^{198}Au has been incorporated into Au NMs for the quantification of their *in vivo* biodistribution *via* measuring the β^- radiation from ^{198}Au decay and Cerenkov luminescence imaging.[16−18] ^{64}Cu, a radioisotope suitable for PET imaging, has been recently integrated with 10 nm CuAu spheric NMs by co-reduction of copper(II) acetylacetonate, gold chloride, and $^{64}CuCl_2$ at 160 °C.[19] However, since the physical properties of Au-based NMs are size and shape dependent, to optimize and expand their *in vivo* biomedical application, a more straightforward, facile, and generally applicable ^{64}Cu labeling method for Au NMs, especially those having near-infrared absorption, is still highly desirable.

In the current work, we integrated ^{64}Cu to a variety of polyethylene glycol (PEG)-stabilized Au NMs of different sizes and shapes *via* chemical reduction of $^{64}CuCl_2$ under mild reaction conditions for immediate use by PET. The labeling efficiency is nearly 100% for all the samples. Our ^{64}Cu-integrated Au NMs ([^{64}Cu]Au NMs) provide an accurate and sensitive localization of NMs with no change of the physical properties of NMs. Using arginine-glycine-aspartic acid (RGD) peptide modified Au nanorods (NRs) as an example, we further proved that these chelator-free NMs have high tumor-targeting ability and can be used for PET image-guided photothermal therapy.

RESULTS AND DISCUSSION

It has been demonstrated previously that Cu could epitaxially grow on metal seeds (such as Au and Pd) to form a core/shell structure.[20,21] Here, we integrated a trace amount of ^{64}Cu onto the as-prepared Au NMs (Figure 1A) by modifying a reported synthesis method of Au/Cu core/shell NPs.[20] Briefly, $^{64}Cu^{2+}$ was reduced by hydrazine (N_2H_4) and grown on the surface of PEG-stabilized Au NMs in the presence of poly(acrylic acid) (PAA). This approach has been successfully applied to a variety of Au NMs with different sizes (10, 30, and 80 nm) and different shapes (sphere, rod, and hexapod). All reactions were carried out at room temperature to maintain the morphology of Au NMs, which would aggregate if heated. A nearly 100% labeling yield was reached within 1 h for all the samples (Figure 1H). In contrast, without the presence of hydrazine, the labeling yield was less than 30% (Figure 1I). We also found that less than 3% ^{64}Cu was released from [^{64}Cu]Au NMs after incubation in phosphate-buffered saline (PBS) for 24 h (Figure S1), which further proved that ^{64}Cu was integrated onto Au NMs instead of simply being trapped inside the PEG layers. The negligible amount of ^{64}Cu (∼ng/mL) compared with Au NMs (∼ mg/mL) did not change the morphology (Figure 1B−G) or the optical property (Figure S2, Table S1) of these samples. Dynamic light scattering (DLS) analysis of amine-PEG-thiol-coated Au NMs indicated about 20 nm increase in diameter, due to polymer coating and the presence of a hydration layer, compared with the "naked" Au NMs (Table S1), while the subsequent ^{64}Cu treatment did not cause a significant hydrodynamic size change. These samples were found to be highly stable in PBS with no visible aggregation after two months (Figure S3).

We first performed *in vivo* PET imaging to investigate the biodistribution of [^{64}Cu]Au NMs. A major concern for PET imaging to monitor the biodistribution of NPs is whether the radionuclide signal could truly reflect the distribution of nanoparticles. Here, we chose 80 nm Au spherical NPs as a model whose *in vivo* pharmacokinetic pattern is obviously different from that of free ^{64}Cu,[22,23] and thus the detachment of free ^{64}Cu should be differentiated. A close look at amine-PEG-thiol (MW = 5000)-modified 80 nm Au NPs before (Figure 2A) and after (Figure 2B) ^{64}Cu treatment demonstrated that the labeling process did not cause a change in morphology. The optical property of ^{64}Cu-integrated 80 nm Au NPs ([^{64}Cu]80 nm Au) is also consistent with 80 nm Au NPs, with a UV absorption peak around 558 nm (Figure 2C). We injected a solution of [^{64}Cu]80 nm Au (150 μg Au, 150 μCi ^{64}Cu) intravenously into mice *via* the tail vein. A solution of ^{64}Cu-chelated 80 nm Au NPs (150 μg of Au, 150 μCi of ^{64}Cu) was used as a comparison. Here, we chose 1,4,7,10-tetraazacyclododecane-*N*,*N*′,*N*″,*N*‴-tetraacetic acid (DOTA) since it is a widely used chelator for ^{64}Cu labeling of nanomaterials.[24−26] The analysis of ^{64}Cu radioactivity in different tissues *via* gamma counting is shown in Figure 2D. The [^{64}Cu]80 nm Au at 24 h postinjection showed a similar radioactivity distribution to traditional ^{64}Cu-chelated 80 nm Au NMs (^{64}Cu-DOTA-80 nm Au) but with higher signal per tissue. Negligible signal was found in the bladder of the mice injected with [^{64}Cu]80 nm Au within 1 h (Figure S4A,B). In contrast, a significantly increased bladder uptake was observed in the mice injected with ^{64}Cu-chelated 80 nm Au. We further collected the urine of mice injected with ^{64}Cu-DOTA-80 nm Au, and negligible Au element was detected by inductively coupled

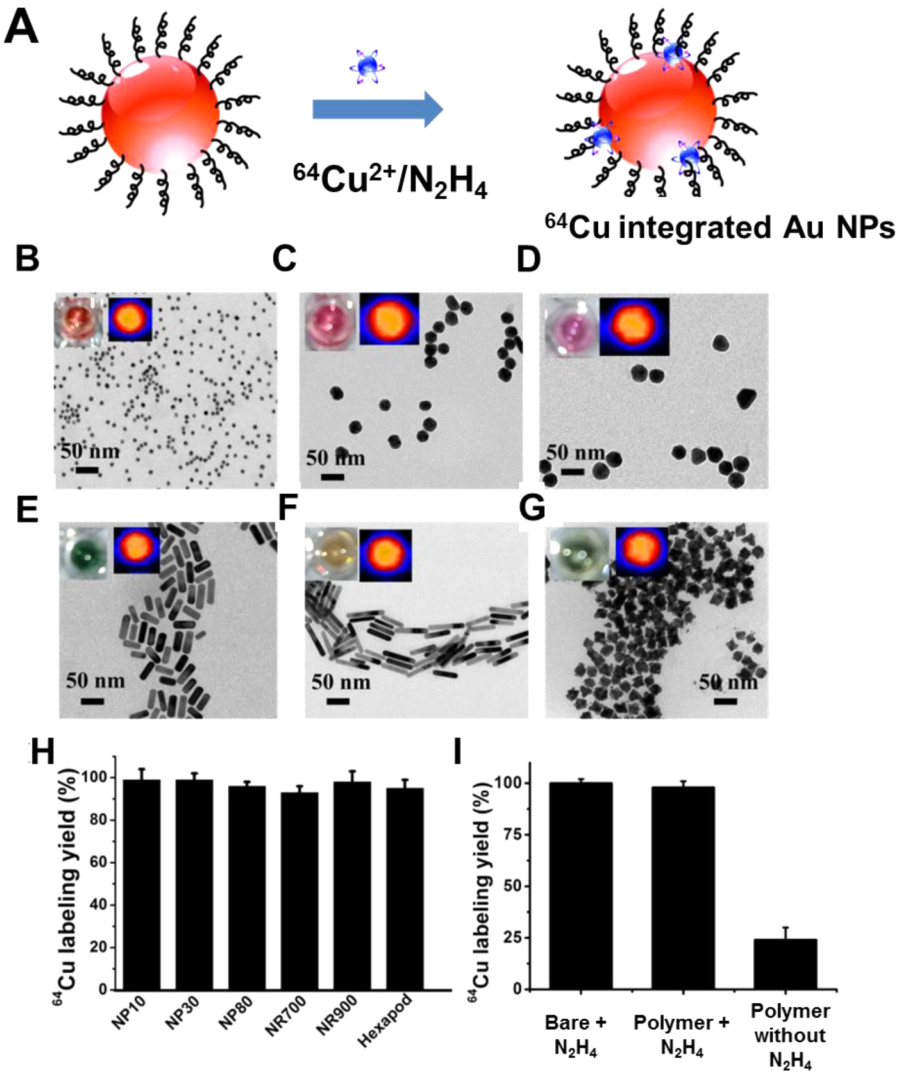

Figure 1. (A) Scheme of synthesis of chelator-free ^{64}Cu-integrated Au NMs. (B–G) TEM images of ^{64}Cu integrated PEGylated 10 nm spherical Au NMs (B), 30 nm spherical Au NMs (C), 80 nm spherical Au NMs (D), 15 × 50 nm Au NRs (E), 15 × 75 nm Au NRs (F), and 30 nm Au nanohexapods (G) after decay. Inset: Photos and PET images of ^{64}Cu-integrated PEGylated Au NMs. (H) ^{64}Cu labeling yield of Au NMs with different shape and size after 1 h reaction at room temperature. (I) ^{64}Cu labeling yield of Au NMs with and without N_2H_4 immediately after preparation.

plasma (ICP) measurements. This is also consistent with the reported fact that the renal clearance threshold is around 5–6 nm,[23] so that 80 nm Au NMs would not be excreted *via* the renal route and free ^{64}Cu would be cleared from the body rapidly. Thus, we assume that the strong radioactivity signal from the bladder of mice within 1 h is due to renal clearance of free $^{64}Cu^{2+}$ trapped in the polymer or ^{64}Cu-chelated polymer that dissociated from the NM in the biological environment. The comparably low signal of ^{64}Cu-DOTA-80 nm Au in previous reports might be due to the partial loss of its radioactivity *via* a rapid renal clearance of free ^{64}Cu. Thus, our ^{64}Cu labeling strategy provides a more reliable way of pinpointing nanoparticle distribution.

To further confirm that the radionuclide signal of our [^{64}Cu]Au NMs could truly reflect the biodistribution of Au NMs, we analyzed the radioactivity and Au NM distribution in various organs. The Au NM distribution was obtained by quantifying the Au amount in the tissue homogenate *via* ICP measurement. The tissue-to-muscle ratio based on Au amount (Table S2) is in a linear correlation with those based on ^{64}Cu radioactivity (Figure 2E, R^2 = 0.954). With the knowledge that both free ^{64}Cu and nanoparticles tend to accumulate in the liver, we specifically investigated whether the radioactivity in the liver is from [^{64}Cu]Au NMs at different time points (Figure 3). Upon injection of the same dose of radioactivity, much higher signal intensity was found in the liver of mice injected with [^{64}Cu]Au NMs than those injected with free ^{64}Cu. We also randomly sacrificed mice at different time points postinjection of [^{64}Cu]Au NMs. The Au amount in the liver homogenate *via* ICP measurement is linearly correlated with the ^{64}Cu radioactivity quantified using gamma counting (Figure 3C, R^2 = 0.923), indicating that the radioactivity at different time points could quantitatively represent [^{64}Cu]Au NMs.

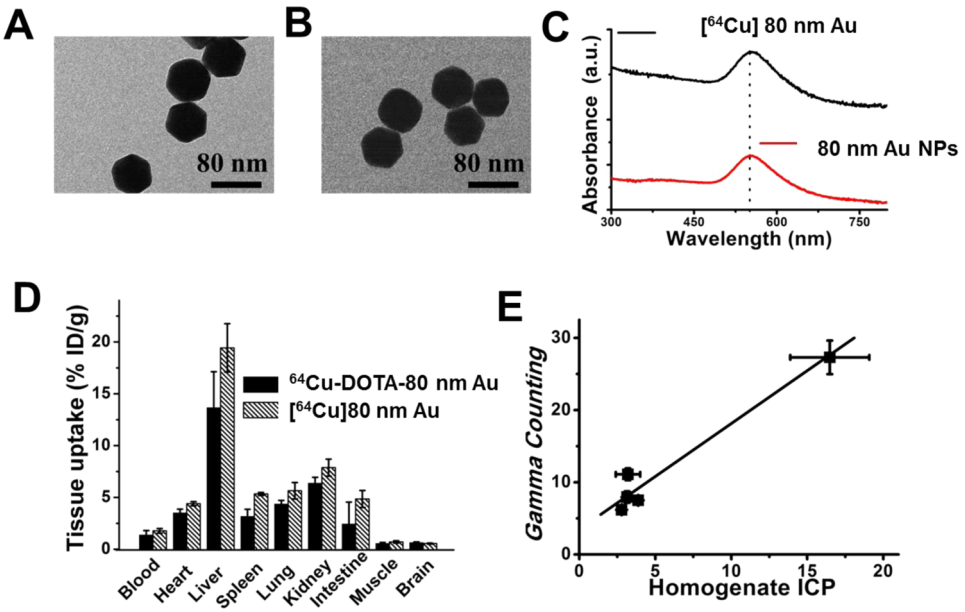

Figure 2. (A, B) TEM of PEGylated 80 nm Au NPs (A) and [^{64}Cu]80 nm Au NPs (B). (C) UV−vis spectra of PEGylated 80 nm Au NPs (red line) and [^{64}Cu]80 nm Au NPs (black line). (D) Biodistribution of the ^{64}Cu-DOTA-80 nm Au (black) *vs* [^{64}Cu]80 nm Au NPs (gradient filled) in mice 24 h postinjection. (E) Correlation among heart-, liver-, spleen-, lung-, and kidney-to-muscle ratios for mice injected with [^{64}Cu]80 nm Au measured *via* gamma countering and tissue homogenate ICP (value in Table S2). $R^2 = 0.954$, $p = 0.0039$.

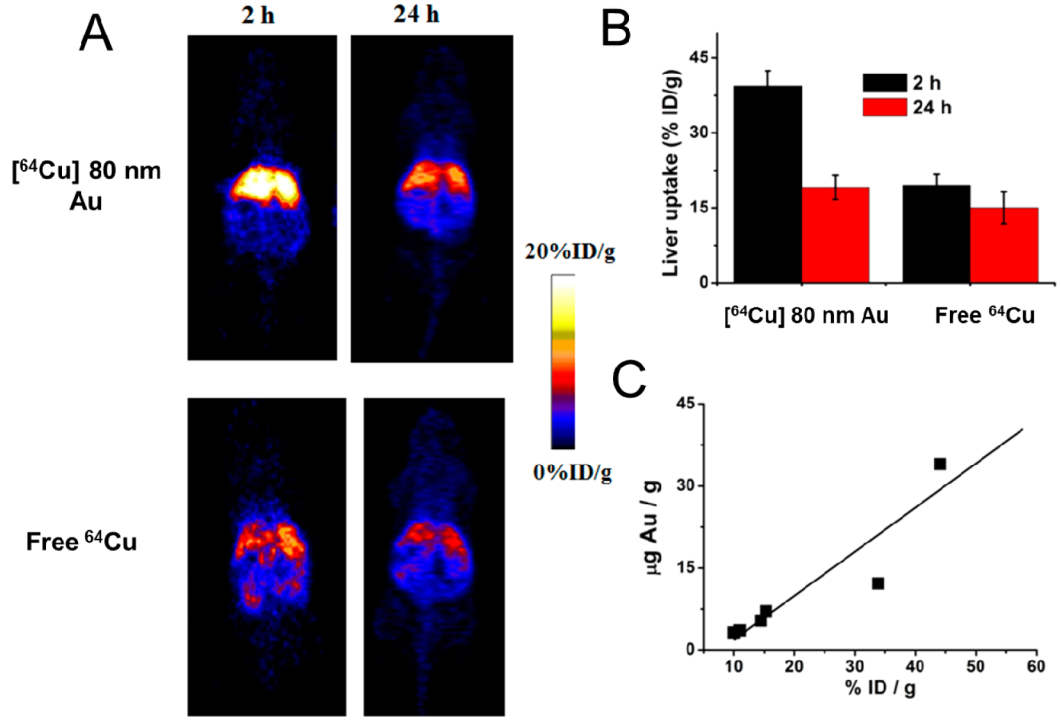

Figure 3. (A) Representative whole-body coronal PET images of mice at 2 and 24 h after intravenous injection of 130 μCi of [^{64}Cu]80 nm Au (upper) as well as free ^{64}Cu(lower) ($n = 3$). (B) Region of interest (ROI) analysis of liver uptake of [^{64}Cu]80 nm Au (upper) as well as free ^{64}Cu ($n = 3$). Upon injection of the same dose of radioactivity, much higher signal intensity was found in the liver of mice injected with [^{64}Cu]Au NMs than those injected with free ^{64}Cu. (C) Correlation among Au per gram liver measured by liver homogenate ICP and liver uptake measured *via* gamma counting. Livers are randomly collected at different postinjection time points. $R^2 = 0.923$.

After verifying the applicability of using [^{64}Cu]Au NMs for *in vivo* biodistribution by PET imaging, we investigated the practicability of using these NMs as multifunctional theranostic agents for PET-guided PTT after iv injection. Here, we used ^{64}Cu-integrated Au nanorods with UV absorption around 808 nm ([^{64}Cu] Au NR808) (Figure 4C) as our model since near-infrared light is preferred as an excitation source in order to

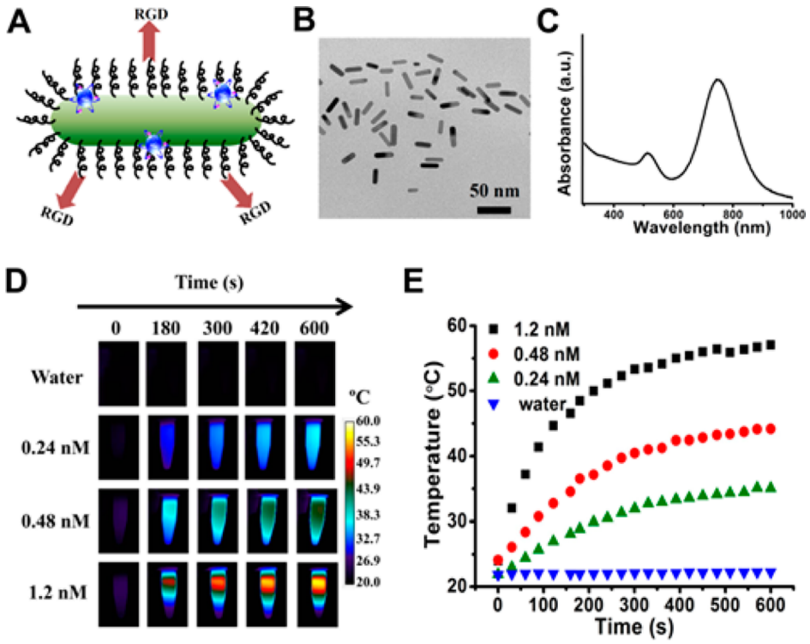

Figure 4. (A) Schematic illustration of the multifunctional Au nanorods (NRs). The NRs were first modified with amine-PEG_{5000}-thiol, then further conjugated with RGD peptide, after which ^{64}Cu was integrated to the Au NRs. (B) TEM and (C) UV−vis spectra of RGD-[^{64}Cu]Au NR808. (D) Temperature mapping during the 808 nm laser irradiation (2 W/cm^2) of an RGD-[^{64}Cu]Au NR808 suspension in distilled water by real-time thermal imaging using a thermal camera (FLIR). (E) Plots of temperature as a function of irradiation time for suspensions of RGD-[^{64}Cu]Au NR808 of different concentrations.

provide deep tissue penetration for biological applications. The Au NRs were commercially available with an average length and width of 25.1 ± 2 nm and 8.0 ± 0.5 nm, respectively (Figure 4B). We first modified the Au NRs with amine-PEG-thiol and then conjugated RGD peptide onto the amine group *via* BS3 cross-linker (details in Materials and Methods). RGD peptide has been reported with integrin-targeting ability toward U87MG human glioblastoma cells (integrin $\alpha v\beta 3$ positive).[27] Then we integrated ^{64}Cu to the modified Au NR808 as indicated in Figure 4A. Prior to *in vivo* application, the photothermal conversion efficiencies of these NRs were tested by measuring the temperature rise of their aqueous suspensions upon laser irradiation. The temperature rise of the solution was mapped by real-time thermal imaging using a thermal camera and analyzed with the IR Flash software. As shown in Figure 4D,E, the temperature of the suspension of these [^{64}Cu]Au NRs (1.2 nM particle concentration, with an extinction of 1.0 at 808 nm) gradually increased with prolonged laser irradiation time, while no obvious temperature change was observed in the pure water control. The rate of temperature increase and the solution temperature at the plateau were directly proportional to particle concentration and laser power (Figure S5). This is consistent with the performance of nonradioactive Au NRs[28,29] and demonstrates that these [^{64}Cu]Au NRs are suitable for photothermal therapy.

The targeting capability of RGD after Cu integration was also assessed. The cell uptake of Cu-treated Au NRs, RGD-Au NRs, and RGD-Au NRs plus free RGD to

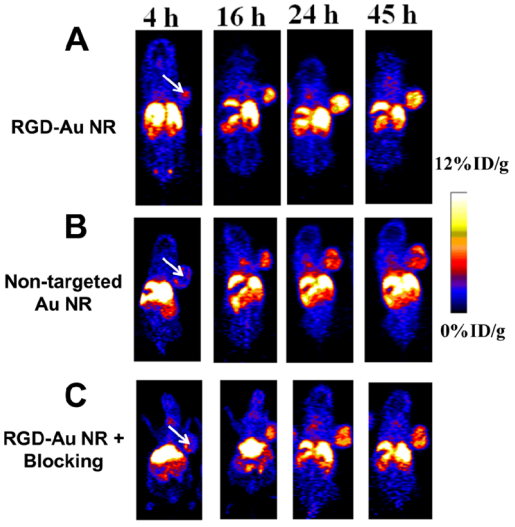

Figure 5. Representative whole-body coronal PET images of U87MG tumor-bearing mice at 4, 16, 24, and 45 h after intravenous injection of 150 μCi of RGD-[^{64}Cu]Au NR808 (A), nontargeting [^{64}Cu]Au NR808 (B), and RGD-[^{64}Cu]Au NR + blocking (C) (n = 3/group). Arrow: tumor area.

block the target (RGD-Au NRs + blocking) by U87MG cells was compared *via* ICP. After incubation for 2 h, the cell uptake of RGD-Au NRs was nearly 2.8 and 3.0 times that of Au NRs and RGD-Au NPs + blocking, respectively (Figure S6). This result indicates that the RGD peptide maintains its integrin-targeting ability toward U87MG cells after Cu treatment.

To demonstrate the feasibility of RGD-[^{64}Cu]Au NR808 for *in vivo* PET-guided photothermal therapy, we injected a solution of these NRs (150 μg of Au,

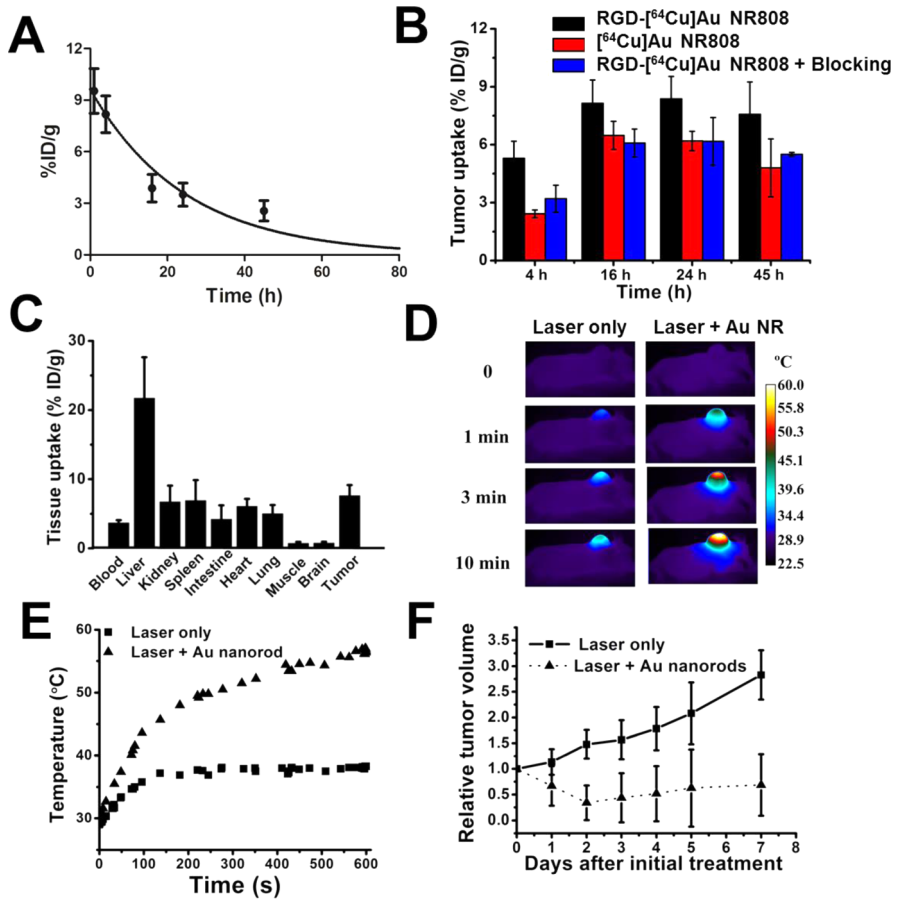

Figure 6. (A) *In vivo* blood terminal half-life ($t_{1/2}$) of RGD-[^{64}Cu]Au NR808. The pharmacokinetic parameters were determined by fitting the data with a two-compartment model. The blood circulation half-time is 17.6 h. (B) Region of interest (ROI) analysis of U87MG tumor uptake of RGD-[^{64}Cu]Au NR808, nontargeting [^{64}Cu]Au NR808, and RGD-[^{64}Cu]Au NR + blocking over time (n = 3/group). (C) Biodistribution of the RGD-[^{64}Cu]Au NR808 in mice bearing U87MG tumors 46 h postinjection (n = 3/group). (D) Temperature mapping of tumor-bearing mice upon laser irradiation for 1, 3, and 10 min with or without intravenous administration of RGD-[^{64}Cu]Au NR808. (E) Plots of average temperature of tumor area as a function of irradiation time with or without administration of RGD-[^{64}Cu]Au NR808. (F) Tumor growth curves of different groups of mice after treatment (n = 4/group).

150 μCi of ^{64}Cu) intravenously into a U87MG xenograft model. In the whole-body PET imaging of mice, liver, spleen, and tumor were all clearly visualized (Figure 5). These RGD-[^{64}Cu]Au NR808 showed a long blood circulation with a half-life of 17 h, which benefits imaging and therapy (Figure 6A). Quantitative ROI analysis showed about 5%ID/g uptake in U87MG tumor at the 4 h time point, which increased to 8%ID/g at 16 h and remained above 7%ID/g even at 45 h (Figure 6B). The tumor uptake of RGD-[^{64}Cu]Au NR808 (8.37 $\pm$ 1.16%ID/g at 24 h postinjection) was higher than that of nontargeted [^{64}Cu]Au NR808 (6.19 $\pm$ 0.5%ID/g) as well as RGD-[^{64}Cu]Au NR808 + blocking (6.17 $\pm$ 1.24%ID/g). Significant NR accumulation in the tumor was further confirmed by the biodistribution data obtained by sacrificing the mice at 45 h postinjection of RGD-[^{64}Cu]Au NR808 and analyzing the ^{64}Cu radioactivity of tissues *via* gamma counting. As shown in Figure 6C, the uptake of tumor (7.6%ID/g) was lower than that of liver (21.7%ID/g), but higher than the other organs. The photothermal treatment was carried out 24 h postinjection when the tumor uptake reached a maximum, as indicated by PET imaging (Figure 5A). The tumor regions were irradiated with a diode laser (808 nm) at a power density of 1.0 W/cm^2 for 10 min. This applied irradiation power and time are based on the tumor uptake of Au NRs indicated by the PET signal. The spot size was adjusted to cover the tumor area. Figure 6D,E summarized the temperature mapping of mice injected with or without RGD-[^{64}Cu]Au NR808 upon laser irradiation. Compared with control mice, which showed ΔT = 9.3 °C, the mice irradiated following injection with RGD-[^{64}Cu]Au NR808 showed a temperature rise of 27.2 °C and reached a plateau within 10 min. This enhanced heating was due to the high tumor uptake and high photothermal conversion efficiency of Au NR808. The elevated temperature is high enough to kill tumor cells *in vivo*. As showed in Figure 6F, the tumor has a negligible reoccurrence after Au NR treatment under laser irradiation, in contrast to an obvious grow path for the tumor treated with laser only.

CONCLUSIONS

We have developed a new method for ^{64}Cu radiolabeling by chemically reducing ^{64}Cu on the surface of PEGylated Au NMs. As the chelator-free ^{64}Cu labeling method in this work is applicable to a variety of Au NMs regardless of the size and shape, Au NMs with high absorption at a certain wavelength could be used for theranostic applications. Integrating ^{64}Cu into Au NMs provides stable radiotracers that can accurately monitor their *in vivo* biodistributions by PET imaging and could help develop photothermal therapeutic protocols more specifically in order to reduce side effects. The nonchelated surface is ready for the conjugation of specific targeting agents, such as peptides and antibodies, which makes these materials even more powerful for cancer-targeted imaging-guided therapy. Labeling ^{64}Cu onto NMs after surface modification and functionalization provides convenience for radioactive material handling and has benefits for potential clinic use.

MATERIALS AND METHODS

Chemicals and Materials. Copper chloride dihydrate ($CuCl_2 \cdot 2H_2O$), poly(acrylic acid) (molecular weight, MW, 5000 g/mol), and hydrazine hydrate (50−60%) were purchased from Sigma-Aldrich. Au NMs were purchased from Nanopartz. Amine-poly(ethylene glycol)-thiol (MW 5000 g/mol) was purchased from Nanocs (New York, NY, USA). BS_3 cross-linker was purchased from Thermo Scientific. Arginine-glycine-aspartic acid peptide, c(RGDyK), was bought from Anaspec. 2,2′,2″-(10-(2-((2,5-Dioxopyrrolidin-1-yl)oxy)-2-oxoethyl)-1,4,7,10-tetraazacyclododecane-1,4,7-triyl)triacetic acid (DOTA-NHS-ester) was purchased from Fisher Scientific. ^{64}Cu was produced by the PET Department, NIH. Deionized (DI) water with a resistivity of 18.0 MΩ was from a Millipore Autopure system. All chemicals were of analytical grade and used without further purification.

Instruments. Transmission electron microscopy (TEM) images were obtained on a FEI Tecnai 12 (120 kV). Samples for TEM analysis were prepared by depositing a drop of diluted NP dispersion on carbon-coated copper grids and dried overnight. UV−vis spectra were obtained by a Genesys 10S UV−vis spectrophotometer. The hydrodynamic diameters of the nanoparticles were measured by a Zetasizer Nano series (Zen3600, Malvern) with Zetasizer 6.0 software as the interface. Inductively coupled plasma atomic emission spectroscopy (ICP-AES) measurements were performed on a JY2000 Ultrace ICP atomic emission spectrometer equipped with a JY AS 421 autosampler and 2400 g/mm holographic grating.

Procedures. *Surface Modification of Au NMs.* A 2 mL amount of Au NMs (260 μg) was centrifuged at 4000−10000 rpm, depending on the size of the materials, for 15 min to remove excess surfactants. The precipitate was collected and redispersed in 2 mL of DI water. Then 2 mg of amine-PEG-thiol was dissolved in 1 mL of water and was added dropwise to the above Au NM aqueous solution. After sonication at room temperature for 1 h, the particles were centrifuged twice to remove excess amine-PEG-thiol and redispersed in water. Dialysis has been carried out before any further conjugation.

Surface Modification of RGD Peptide. A 2 nmol portion of PEGylated Au NMs was dispersed in 2 mL of borate buffer (pH 8.2). Then 10 μL of BS_3 cross-linker (10 mg/mL) was added to the solution. After stirring for 30 min at room temperature, the mixture was collected *via* centrifugal filter (30 k cutoff) and redispersed in DI water. The particles were then washed and collected *via* centrifugation three times before finally dispersing in borate buffer. Subsequently, 0.1 mL of RGD peptide (2 mg/mL) was added to the particle solution. The mixture was then stirred overnight at room temperature. The final product was purified by dialysis bag (100k cutoff).

Preparation of [^{64}Cu] Au NMs. A 10 μmol sample of PAA was added into 1 mL amine-PEG-thiol-capped Au NMs. As received $^{64}CuCl_2$ was diluted into 0.4 M ammonium acetate buffer (NH_4Ac, pH 5.5). A 20 μCi ^{64}Cu solution was then added dropwise into the Au NM solution. After stirring for 5 min, 3 μmol of N_2H_4 was added, and the solution was allowed to react at room temperature for 1 h before it was washed by centrifugation to remove the excess reagents as well as the unreacted ^{64}Cu. The labeling efficiency was calculated on the basis of the radiation dosimeter readings before and after purification.

Preparation of ^{64}Cu-DOTA-Au NMs. A 2 nmol amount of PEGylated Au NMs was dispersed in 2 mL of borate buffer, and 1 mg of NHS-DOTA was added to the solution. After reaction at room temperature overnight, the solution was purified by a dialysis bag (100k cutoff) to remove excess NHS-DOTA. Details regarding ^{64}Cu labeling have been reported elsewhere.[30−32] Briefly, $^{64}CuCl_2$ in 0.4 M ammonium acetate buffer (NH_4Ac, pH 5.5) was added to the solution of DOTA-labeled NMs. After incubation for 1 h with constant shaking, the solution was purified by centrifugal filter (100k cutoff) to remove free ^{64}Cu. The filtered solution was monitored by radiation dosimeter until no radioactivity in the supernatant was measured.

Cell Culture and Animal Model. All animal work was performed following a protocol approved by the National Institutes of Health Clinical Center Animal Care and Use Committee (NIH CC/ACUC). The U87MG human glioblastoma cell line was purchased from the American Type Culture Collection (ATCC) and was cultured in ATCC-formulated Eagle's minimum essential medium (EMEM) with 10% (v/v) fetal bovine serum at 37 °C with 5% CO_2. Athymic nude mice purchased from Harlan (Indianapolis, IN, USA) were subcutaneously implanted with 1×10^5 U87MG cells in the shoulder. The *in vivo* imaging and photothermal treatment was performed after the tumor volume reached around 100 mm^3.

Cell Uptake Experiment. U87MG cells were cultured in a T75 culture flask. Before the uptake experiment, the growth medium was removed. The cells were washed twice with PBS and incubated with the culture medium containing the PEGylated Au NMs, RGD-PEGylated Au NMs, or RGD-PEGylated Au NMs with a blocking dose of RGD (1 mg, 1 h), respectively. After 2 h, the cells were washed three times with cold PBS and treated with 0.2 mL of trypsin solution (containing 0.25% EDTA). The cell number was counted with a hematocytometer. The cell pellets were digested with aqua regia until the solution was completely clear. The Au amount was measured by ICP-AES.

Small-Animal Positron Emission Tomography Imaging. The details of small-animal PET imaging and region-of-interest (ROI) analysis have been reported before.[32,33] The U87MG tumor-bearing mice were first anesthetized with isoflurane (Abbott Laboratories), and then each was intravenously injected with 150 μCi [^{64}Cu]Au NMs or RGD-[^{64}Cu]Au NMs. Another group of mice were each injected with 6 mg of RGD at 1 h before RGD-[^{64}Cu]Au NM administration. PET scans and imaging analysis were carried out on an Inveon microPET scanner (Siemens Medical Solutions) at different postinjection time points. Three-dimensional ROIs were drawn over the tumor and organs on decay-corrected whole-body coronal images for each PET scan. The average radioactivity concentration was obtained from the mean pixel values within the ROI volume, which was converted to counts per milliliter per minute by using a predetermined conversion factor.[32,33] The counts per milliter per minute were converted to counts per gram per minute based on the assumption that the tissue density is 1 g/mL, and the values were divided by the injected dose to obtain the imaging ROI-derived percentage injected dose per gram (%ID/g).

Biodistribution Study. The mice were sacrificed at 45 h post-injection after the last scan. Organs of interest were collected and weighed, and the radioactivity was measured in a well gamma-counter (Wallach Wizard, PerkinElmer, Waltham, MA, USA). The uptake of ^{64}Cu in the various organs was calculated as the percentage of the injected dose per gram of tissue according to the prepared standards. The weighed organs were then immersed in digest solution (HNO_3/HCl = 1:1) with a volume of 5 mL. The dispersions were heated to boiling until organs were completely dissolved. A 1 mL amount of H_2O_2 was then added into the solution, and heating continued until the solution became clear and transparent. The solution was then cooled to room temperature, diluted by 2% HNO_3 to 10 mL, and subsequently analyzed by ICP to determine the concentration of Au in each sample.

Photothermal Treatment with NIR Light. The aqueous Au NM solutions with different concentrations were irradiated with an 808 nm NIR laser (LaserGlow Technologies) under different powers. Real-time thermal imaging of the solution was recorded using a thermal camera (FLIR). The quantitative analysis was performed with FLIR Examiner software.

For *in vivo* studies, mice bearing U87MG tumors were intravenously injected with 150 μCi [^{64}Cu]Au NMs. After 24 h PET scanning, the tumor area was irradiated with the 808 nm NIR laser at a power density of 1 W cm^{-2} for 10 min. Mice treated with laser only were used as a control. Real-time thermal imaging of U87MG tumors was monitored with FLIR. After treatment, the tumor volume was monitored by measuring the tumor dimensions at various time points using a caplier. Tumor volume (V) (mm^3) was calculated using the following formula: $V = ab^2/2$, where a refers to the length and b refers to the width in millimeters, respectively. Relative tumor volumes were calculated as tumor volume at different time point divided by the original tumor volume.

Conflict of Interest: The authors declare no competing financial interest.

Supporting Information Available: Additional information and figures. This material is available free of charge *via* the Internet at http://pubs.acs.org.

Acknowledgment. This work is supported by the Intramural Research Program (IRP) of the NIBIB, NIH.

REFERENCES AND NOTES

1. Jaffray, D. A. Image-Guided Radiotherapy: From Current Concept to Future Perspectives. *Nat. Rev. Clin. Oncol.* **2012**, *9*, 688–699.
2. Kircher, M. F.; Zerda, A.; Jokerst, J. V.; Zavaleta, C. L.; Kempen, P. J.; Mittra, E.; Pitter, K.; Huang, R.; Campos, C.; Habte, F.; *et al*. A Brain Tumor Molecular Imaging Strategy Using a New Triple-Modality MRI-Photoacoustic-Raman Nanoparticle. *Nat. Med.* **2012**, *18*, 829–834.
3. Fass, L. Imaging and Cancer: A Review. *Mol. Oncol.* **2008**, *2*, 115–152.
4. Dreaden, E. C.; Mackey, M. A.; Huang, X.; Kang, B.; El-Sayed, M. A. Beating Cancer in Multiple Ways Using Nanogold. *Chem. Soc. Rev.* **2011**, *40*, 3391–3404.
5. Dreaden, E. C.; Alkilany, A. M.; Huang, X.; Murphy, C. J.; El-Sayed, M. A. The Golden Age: Gold Nanoparticles for Biomedicine. *Chem. Soc. Rev.* **2012**, *41*, 2740–2779.
6. Murphy, C. J.; Gole, A. M.; Stone, J. W.; Sisco, P. N.; Alkilany, A. M.; Goldsmith, E. C.; Baxter, S. C. Gold Nanoparticles in Biology: Beyond Toxicity to Cellular Imaging. *Acc. Chem. Res.* **2008**, *41*, 1721–1730.
7. Gambhir, S. S. Molecular Imaging of Cancer with Positron Emission Tomography. *Nat. Rev. Cancer* **2002**, *2*, 683–693.
8. Czernin, J.; Ta, L.; Herrmann, K. Does PET/MRI Imaging Improve Cancer Assessments? Literature Evidence from More Than 900 Patients. *J. Nucl. Med.* **2014**, *55* (Suppl. 2), 59S–62S.
9. Wang, F.; Wang, Z.; Hida, N.; Kiesewetter, D. O.; Ma, Y.; Yang, K.; Rong, P.; Liang, J.; Tian, J.; Niu, G.; *et al*. A Cyclic HSV1-TK Reporter for Real-Time PET Imaging of Apoptosis. *Proc. Natl. Acad. Sci. U.S.A.* **2014**, *111*, 5165–5170.
10. Shokeen, M.; Anderson, C. J. Molecular Imaging of Cancer with Copper-64 Radiopharmaceuticals and Positron Emission Tomography (PET). *Acc. Chem. Res.* **2009**, *42*, 832–841.
11. Cutler, C. S.; Hennkens, H. M.; Sisay, N.; Markai, S. H.; Jurisson, S. S. Radiometals for Combined Imaging and Therapy. *Chem. Rev.* **2013**, *113*, 858–883.
12. Wadas, T. J.; Wong, E. H.; Weisman, G. R.; Anderson, C. J. Coordinating Radiometals of Copper, Gallium, Indium, Yttrium and Zirconium for PET and SPECT Imaging of Disease. *Chem. Rev.* **2010**, *110*, 2858–2902.
13. Shukla, R.; Chanda, N.; Zambre, A.; Upendran, A.; Katti, K.; Kulkami, R. R.; Nune, S. K.; Casteel, S. W.; Smith, C. J.; Vimal, J.; *et al*. Laminin Receptor Specific Therapeutic Gold Nanoparticles (^{198}AuNP-EGCg) Show Efficacy in Treating Prostate Cancer. *Proc. Natl. Acad. Sci. U.S.A.* **2012**, *109*, 12426–12431.
14. Liu, T. W.; MacDonald, T. D.; Shi, J.; Wilson, B. C.; Zheng, G. Intrinsically Copper-64-Labeled Organic Nanoparticles as Radiotracers. *Angew. Chem., Int. Ed.* **2012**, *51*, 13128–13131.
15. Liu, T. W.; MacDonald, T. D.; Jin, C. S.; Gold, J. M.; Bristow, R. G.; Wilson, B. C.; Zheng, G. Inherently Multimodal Nanopartcle-Driven Tracking and Real-Time Delineation of Orthotopic Prostate Tumors and Micrometastases. *ACS Nano* **2013**, *7*, 4221–4232.
16. Wang, Y.; Liu, Y.; Luehmann, H.; Xia, X.; Wan, D.; Cutler, C.; Xia, Y. Radioluminescent Gold Nanocages with Controlled Radioactivity for Real-Time *in Vivo* Imaging. *Nano Lett.* **2013**, *13*, 581–585.
17. Black, K. C. L.; Wang, Y.; Luehmann, H. P.; Cai, X.; Xing, W.; Pang, B.; Zhao, Y.; Cutler, C. S.; Wang, L. V.; Liu, Y.; *et al*. Radioactive ^{198}Au-Doped Nanostructures with Different Shapes for *in Vivo* Analyses of Their Biodistribution, Tumor Uptake, and Intratumoral Distribution. *ACS Nano* **2014**, *8*, 4385–4394.
18. Zhou, C.; Hao, G. Y.; Thomas, P.; Liu, J. B.; Yu, M. X.; Sun, S. S.; Oz, O. K.; Sun, X. K.; Zheng, J. Near-Infrared Emitting Radioactive Gold Nanoparticles with Molecular Pharmacokinetics. *Angew. Chem., Int. Ed.* **2012**, *51*, 10118–10122.
19. Zhao, Y.; Sultan, D.; Detering, L.; Cho, S.; Sun, G.; Pierce, R.; Wooley, K. L.; Liu, Y. Copper-64-Alloyed Gold Nanoparticles for Cancer Imaging: Improved Radiolabel Stability and Diagnostic Accuracy. *Angew. Chem., Int. Ed.* **2014**, *53*, 156–159.
20. Alvarez-Paneque, A. F.; Rodriguez-Gonzalez, B.; Pastoriza-Santos, I.; Liz-Marzan, L. M. Shape-Templated Growth of Au@Cu Nanoparticles. *J. Phys. Chem. C* **2013**, *117*, 2474–2479.
21. Jin, M.; Zhang, H.; Wang, J.; Zhong, X.; Lu, N.; Li, Z.; Xie, Z.; Kim, M. J.; Xia, Y. Copper Can Still Be Epitaxially Deposited on Palladium Nanocrystals to Generate Core-Shell Nanocubes Despite Their Large Lattice Mismatch. *ACS Nano* **2012**, *6*, 2566–2573.
22. Longmire, M.; Choyke, P. L.; Kobayashi, H. Clearance Properties of Nano-Sized Particles and Moleculars as Imaging Agents: Considerations and Caveats. *Nanomedicine* **2008**, *3*, 703–717.
23. Choi, H. S.; Liu, W.; Misra, P.; Tanaka, E.; Zimmer, J. P.; Ipe, B. I.; Bawendi, M. G.; Frangioni, J. V. Renal Clearance of Nanoparticles. *Nat. Biotechnol.* **2007**, *25*, 1165–1170.
24. Cai, W.; Chen, K.; Li, Z.; Gambhir, S. S.; Chen, X. Dual-Function Probe for PET and Near-Infrared Fluorescence Imaging of Tumor Vasculature. *J. Nucl. Med.* **2007**, *48*, 1862–1870.
25. Xie, J.; Chen, K.; Huang, J.; Lee, S.; Wang, J.; Gao, J.; Li, X.; Chen, X. PET/NIRF/MRI Triple Functional Iron Oxide Nanoparticles. *Biomaterials* **2010**, *31*, 3016–3022.
26. Kotagiri, N.; Niedzwiedzki, D. M.; Ohara, K.; Achilefu, S. Activatable Probes Based on Distance-Dependent Luminescence Associated with Cerenkov Radiation. *Angew. Chem., Int. Ed.* **2013**, *52*, 7756–7760.
27. Cai, W.; Shin, D.; Chen, K.; Gheysens, O.; Cao, Q.; Wang, S. X.; Gambhir, S. S.; Chen, X. Peptide-Labeled Near-Infrared Quantum Dots for Imaging Tumor Vasculature in Living Subjects. *Nano Lett.* **2006**, *6*, 669–676.

28. Wang, Y.; Black, K. C. L.; Luehmann, H.; Li, W.; Zhang, Y.; Cai, X.; Wan, D.; Liu, S.; Li, M.; Kim, P.; *et al*. Comparison Study of Gold Nanohexapods, Nanorods, and Nanocages for Photothermal Cancer Treatment. *ACS Nano* **2013**, *7*, 2068–2077.
29. Dickerson, E. B.; Dreaden, E. C.; Huang, X.; El-Sayed, I. H.; Chu, H.; Pushpanketh, S.; McDonald, J. F.; El-Sayed, M. A. Gold Nanorod Assisted Near-Infrared Plasmonic Photothermal Therapy (PPTT) of Squamous Cell Carcinoma in Mice. *Cancer Lett.* **2008**, *269*, 57–66.
30. Huang, X.; Zhang, F.; Lee, S.; Swierczewska, M.; Kiesewetter, D. O.; Lang, L.; Zhang, G.; Zhu, L.; Gao, H.; Choi, H.; *et al*. Long-Term Multimodal Imaging of Tumor Draining Sentinel Lymph Nodes Using Mesoporous Silica-Based Nanoprobes. *Biomaterials* **2012**, *33*, 4370–4378.
31. Jacobson, O.; Weiss, I. D.; Szajek, L. P.; Niu, G.; Ma, Y.; Kiesewetter, D. O.; Farber, J. M.; Chen, X. PET Imaging of CXCR4 Using Copper-64 Labeled Peptide Antagonist. *Theranostic* **2011**, *1*, 251–262.
32. Cai, W.; Olafsen, T.; Zhang, X.; Cao, Q.; Gambhir, S. S.; Williams, L. E.; Wu, A. M.; Chen, X. PET Imaging of Colorectal Cancer in Xenograft-Bearing Mice by Use of an ^{18}F-Labeled T84.66 Anti-Carcinoembryonic Antigen Diabody. *J. Nucl. Med.* **2007**, *48*, 304–310.
33. Cai, W.; Wu, Y.; Chen, K.; Cai, Q.; Tice, D. A.; Chen, X. *In Vitro* and *in Vivo* Characterization of ^{64}Cu-Labeled Abegrin^{TM}, a Humanized Monoclonal Antibody against Integrin $\alpha v\beta 3$. *Cancer Res.* **2006**, *66*, 9673–9681.